

Direct observation of hidden spin polarization in $2H$ -MoTe₂J. Tu,^{1,*} X. B. Chen,^{2,*} X. Z. Ruan,^{1,†} Y. F. Zhao,¹ H. F. Xu,¹ Z. D. Chen,¹ X. Q. Zhang,¹ X. W. Zhang,^{2,‡} J. Wu,³ L. He,¹ Y. Zhang,⁴ R. Zhang,¹ and Y. B. Xu^{1,3,§}¹*Jiangsu Provincial Key Laboratory of Advanced Photonic and Electronic Materials, Collaborative Innovation Center of Advanced Microstructures, School of Electronic Science and Engineering, Nanjing University, Nanjing, 210093, China*²*Shenzhen Key Laboratory of Flexible Memory Materials and Devices, College of Electronic Science and Technology, Shenzhen University, Nantian Ave. 3688, Shenzhen, Guangdong 518060, China*³*York-Nanjing Joint Center in Spintronics, Department of Electronic Engineering and Department of Physics, The University of York, York, YO10 5DD, United Kingdom*⁴*Central Laser Facility, STFC Rutherford Appleton Laboratory, Didcot OX11 0QX, United Kingdom*

(Received 17 August 2019; revised manuscript received 29 November 2019; published 3 January 2020)

Centrosymmetric (CS) nonmagnetic materials with hidden spin polarization induced by non-CS site symmetries and spin-orbit coupling are promising candidates for spintronic applications, in light of the zero net spin polarization and modulatable spin effects hidden in the local structures. There is, however, an open issue regarding the possible spin splitting induced by broken inversion symmetry at the sample surface. Here, we performed combinatorial experimental and theoretical studies on the potentially hidden spin polarization in $2H$ -MoTe₂ and its mechanism. A large spin splitting of 236 meV and opposite spin polarizations up to 80% along out-of-plane direction (z axis) in K and K' valleys were observed from both spin- and angle-resolved photoemission spectroscopy (spin-ARPES) and density functional theory (DFT). We further found from the DFT calculations that a medium dipole field mimicked the surface symmetry breaking in ARPES measurements induces negligible variation of spin polarization. Our study demonstrates the existence of the intrinsic hidden spin effects in $2H$ -MoTe₂ and opens a way of utilizing these effects in spintronic devices.

DOI: [10.1103/PhysRevB.101.035102](https://doi.org/10.1103/PhysRevB.101.035102)**I. INTRODUCTION**

Spin polarization in nonmagnetic materials originates from the break of inversion crystalline symmetry [1–5] that could occur globally [1,2] or locally [3–6]. Such spin polarization can induce an effective magnetic field [7] for operating electron's spin in the absence of magnetic ions or field. At the same time, two-dimensional transition metal dichalcogenides (TMDCs) are promising materials for new-generation electronic devices with several virtues including direct band gap [8–12], superconductivity [13,14], ideal Van der Waals heterostructures [15], and valleytronics [15–18]. Spin splitting [19–22] has been observed in the K valley of inversion asymmetric TMDC structures that are interlocked [14,23,24] with the coexisted valley polarization effect [16–18]. Whereas in the centrosymmetric TMDC structures, a new type of spin effect, i.e., the hidden spin polarization [5], also known as layer-locked hidden spin texture in layered materials [3], has been observed [4,25–28]. Although it is well established that the optical properties of inversion symmetric TMDC systems

[29–31] are qualitatively affected by their hidden spin texture, a concern that the observed hidden spin texture [4,25–28] might be mainly induced by the broken inversion symmetry in experiments was raised recently [32]. Therefore it is critical to perform combined experimental and theoretical studies on centrosymmetric TMDC materials such as $2H$ -MoTe₂ to explore the mechanism of the hidden spin polarization [5].

MoTe₂ possesses intriguing physical properties, including type-II topological Weyl semimetal phase [33], spin splitting [28], and valleytronics [34]. It can be stabilized near room temperature in three types of crystal structures, namely, the $2H$ (hexagonal) [35], $1T'$ (monoclinic) [36], and T_d (orthorhombic) [33] phases. The tunability of crystal structures (from $2H$ to $1T'$ [35] and from $1T'$ to T_d – MoTe₂ [28]) and the corresponding physical properties in MoTe₂ offers an opportunity to build Ohmic homojunction contact [37], making it an ideal platform for two-dimensional electronic devices. Here, we focus on the spintronic properties of the highly symmetrical semiconducting phase of MoTe₂, i.e., the centrosymmetric hexagonal $2H$ phase with potentially hidden spin polarization. By using spin-ARPES, we observed strong net spin polarizations on the surface of $2H$ -MoTe₂, which have opposite polarization directions in the K versus K' valleys of the hexagonal lattice. We tested the two possible origins of the measured spin polarization via combinatorial theoretical and experimental studies: (i) the weak surface dipole field due to the breaking of bulk inversion symmetry and (ii) the layer-locked hidden spin polarization. We find that the evaluated spin texture (polarization directions) in

*These authors contributed equally to this work.

†Correspondence and requests for materials should be addressed to: xzruan@nju.edu.cn

‡Correspondence and requests for materials should be addressed to: xiuwenzhang@szu.edu.cn

§Correspondence and requests for materials should be addressed to: ybxu@nju.edu.cn

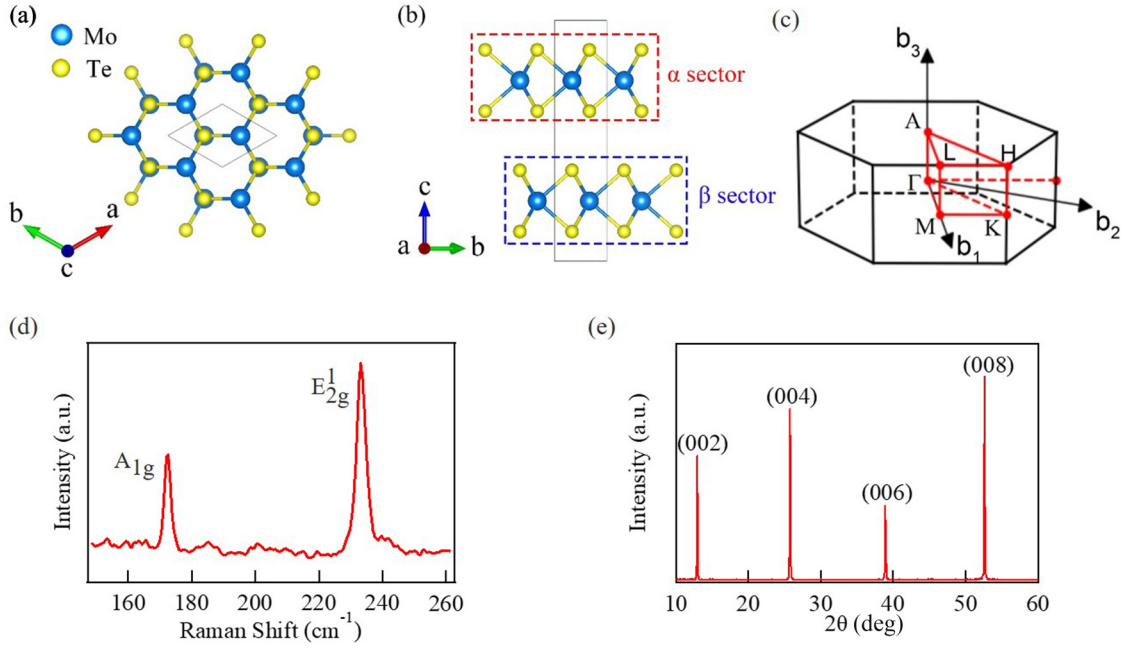


FIG. 1. (a) Top and (b) side views of the lattice structure. The upper and lower layers in the unit cell denoted as α and β sectors are inversion partners. (c) Brillouin zone of $2H$ - MoTe_2 in reciprocal space. (d) Raman signal of $2H$ - MoTe_2 . A_{1g} and E_{2g}^1 denote the phonon modes of $2H$ - MoTe_2 . (e) XRD pattern of $2H$ - MoTe_2 .

the situation with broken symmetry in the appearance of a medium surface dipole field are analogous to that in the centrosymmetric structure. For both cases, the calculated spin polarizations are nearly identical and both agree well with the measured spin polarization. This shows that the contribution of the symmetry-breaking surface dipole field to the measured spin polarization is negligible. Our combined experimental and theoretical studies thus reveal the existence of the intrinsic hidden spin polarization in centrosymmetric materials.

II. EXPERIMENTAL DETAILS

$2H$ - MoTe_2 sample was synthesized by the CVT method. High-purity Mo and Te powders were mixed with a mole ratio in a quartz tube. Under the pressure less than 0.1 Pa, the tube was heated to 700°C within 12 hours, maintained at this temperature for 3 days and then cooled down to room temperature within 12 hours, to get MoTe_2 polycrystalline powder. TeCl_4 powder was used as the transporting agent to be mixed with MoTe_2 powder in a new quartz tube. The tube was heated to 1040°C within 2 hours, maintained for 5 days, and then cooled down to room temperature within 12 hours, yielding $2H$ - MoTe_2 single crystal.

The electronic band structure measurements were conducted on ARPES system with a SPECS PHOIBOS150 hemispherical energy analyzer. The base pressure of the analyzer chamber is 2×10^{-10} mbar. A helium lamp is used to generate ultraviolet photons with an energy of 21.218 eV (He-I). The angular resolution of the system is 0.05° and the energy resolution is 35 meV at room temperature. The sample was cleaved in situ in an ultrahigh vacuum chamber (4×10^{-8} mbar) by using a scotch tape to obtain clean surface. Spin detection is realized by using a Micro-Mott spin detector that includes a strong spin-orbital coupling target (thorium),

and four channel electron multipliers to collect the scattered electrons. A small circular aperture is chosen to confine the photoelectrons from the same point of reciprocal space.

III. EXPERIMENTAL RESULTS

Figures 1(a) and 1(b) display the lattice structure of $2H$ - MoTe_2 (space group: $P6_3/mmc$) on top and side views, respectively. Figure 1(c) shows the Brillouin zone of $2H$ - MoTe_2 in reciprocal space. The molybdenum layer is sandwiched between two layers of tellurium within one monolayer, and each atom is surrounded by three atoms of another type. The Te-Mo-Te slabs are bonded with each other by Van der Waals forces by the stacking pattern shown in Fig. 1(b). The planar structures of up and down monolayers are related to each other by a rotation of 180° , constituting an inversion symmetric unit cell. It crystallizes in a trigonal prismatic arrangement with an in-plane lattice constant of 3.517 \AA and an out-of-plane lattice constant of 13.962 \AA [38]. Raman spectrum measured with a laser of the wavelength of 514 nm, under normal pressure and room temperature, is included in Fig. 1(d), which demonstrates two phonon oscillation modes, A_{1g} at 172.65 cm^{-1} and E_{2g}^1 at 233.15 cm^{-1} , corresponding to the characteristic out-of-plane and in-plane phonon modes, respectively. The crystal structure of $2H$ - MoTe_2 was investigated using high-resolution x-ray diffraction (XRD) with $\text{Cu K}\alpha$ radiation ($\lambda = 1.5418 \text{ \AA}$). Figure 1(e) presents the result of the XRD out-of-plane $\theta - 2\theta$ scan for the $2H$ - MoTe_2 sample. A group of diffraction peaks are clearly observed at 12.94° , 25.74° , 38.88° , and 52.58° , which are corresponding to the (002), (004), (006), and (008) planes of $2H$ - MoTe_2 , respectively [36].

Figure 2(a) shows the valence-band structure along $M - K - \Gamma - M$ [Fig. 1(c)] at room temperature. The valence-

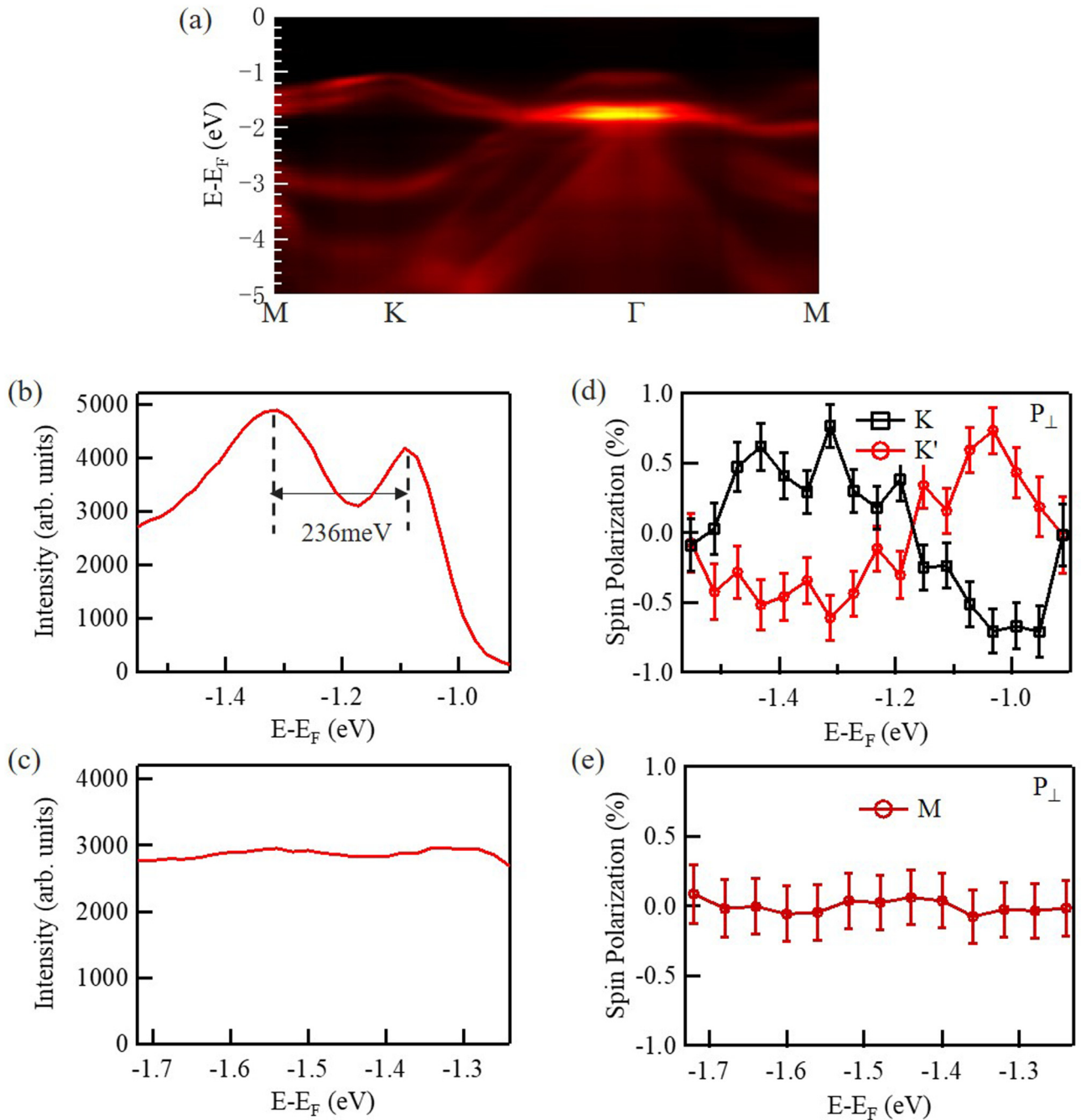


FIG. 2. (a) Electronic band structure of $2H$ - MoTe_2 along the high-symmetry points $M - K - \Gamma - M$ acquired from ARPES. [(b) and (c)] EDC at K and M . Spin splitting of 236 meV at K valley is displayed in (b). [(d) and (e)] Spin polarizations vertical to the sample plane at $K(K')$ and M . In (d), black and red curves correspond to K and K' , respectively.

band maximum of $2H$ - MoTe_2 at K and Γ are rather close to each other, which is much different from MoS_2 [8] and MoSe_2 [39]. This will be an advantage for the applications in the field of hole-type spin based devices [40]. Band structure along $K - \Gamma - K'$ (see Fig. S1 [41]) reveals symmetry pattern except for the different intensities along two directions, because of the photoemission matrix element effects. The band splitting at K point is 236 meV, as shown in Fig. 2(b), which is larger than that of MoS_2 and MoSe_2 , implying stronger spin-orbit interaction. We will prove that the symmetric valleys lo-

ating at K and K' have inverse spin polarizations within each monolayer.

The energy distribution curves (EDC) at K and M point are shown in Figs. 2(b) and 2(c), respectively. One can clearly see that there are two energy distribution peaks corresponding to the first and second valence bands at K point. There is a large splitting of 236 meV between two peaks in the EDC curve around K valley as shown clearly in Fig. 2(b). The EDC at K' is identical to that at K point. Figure 2(c) demonstrates that the peaks become broadening at M point. The measured spin

polarizations around $K(K')$ and M are shown in Figs. 2(d) and 2(e), respectively. Since the escape depth of photoelectrons from $K(K')$ valley is about 6 Å with the photon energy of 21.218 eV [49], which is less than the out-of-plane lattice constant 13.962 Å, most photoelectrons come from the first layer. Therefore the spin polarization results should represent the topmost monolayer with very little contributions from the lower layers.

The spin polarizability detected by spin-ARPES is defined as

$$P = \frac{1}{S_{\text{eff}}} \frac{I_+ - I_-}{I_+ + I_-}. \quad (1)$$

The value of S_{eff} is 0.16 ± 0.01 , which is the effective Sherman function determined by the spin-ARPES system. I_+ and I_- are the intensity acquired by the two channeltrons at opposite directions. Spin polarizations vertical to the sample plane at K and K' are demonstrated in Fig. 2(d). The polarization at K is opposite to that at K' with the same level, verifying the completeness of time reversal-symmetry and no net magnetic momentum existing. The large spin polarization of 80% at K and K' has proven pure spin splitting at these two valleys, coinciding with type II Dresselhaus effect [5]. In-plane spin polarization data at K and K' are shown in Fig. S2 [41], which demonstrate negligible spin polarization. Considering the geometry of the system as shown in Fig. S3 and nonpolarized photons used during spin-ARPES measurements [41], the influence to the spin polarization vertical to the sample surface due to the matrix element effect [50,51] can be estimated to be around 6%–12%, which is much smaller compared to the spin polarization of 80% observed. Therefore the spin polarization detected represents the intrinsic spin polarization at K and K' . However, with the breaking of inversion symmetry at sample surface, vertical dipole in $2H\text{-MoTe}_2$ could be another cause of the observed spin polarization. No net spin polarization along vertical direction exists at M point, as shown in Fig. 2(e), suggesting that the spin polarized states are also regulated in momentum space, coinciding with the results of WSe_2 [29]. The large spin polarization observed experimentally demonstrates that there exists inverse net spin splitting around K and K' valleys, indicating the inequivalence of the two valleys within the topmost monolayer.

IV. DFT CALCULATIONS

To reveal the origin of the above measured spin splitting, we conducted theoretical evaluations on the electronic structure and spin polarization of $2H\text{-MoTe}_2$ in the framework of DFT [41]. Figure 3(a) shows the calculated orbital-projected band structure of bulk $2H\text{-MoTe}_2$, illustrating that the majority components of the first two valence bands (VB1 and VB2) at K valley are $Mo-d$ states. The experimentally measured valence-band structure [Fig. 2(a)] is rather similar to the calculated valence band of bulk materials, indicating that the surface effect in experiments is ignorable. The calculated energy difference between VB1 and VB2 at K valley of $2H\text{-MoTe}_2$ is 283 meV, slightly higher than the experimental value of 236 meV, but smaller than the measured spin splitting in WSe_2 [4], suggesting that the spin splitting is mainly related to the M site in MX_2 (W has larger SOC than Mo whereas

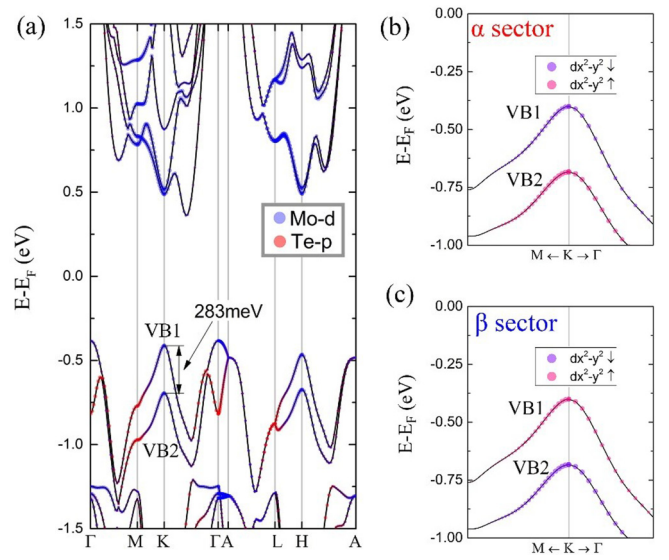


FIG. 3. (a) Evaluated band structure of bulk $2H\text{-MoTe}_2$ by DFT+SOC. The dotted lines with different colors denote the band projection onto different atomic orbitals, indicating that the first two valence bands (VB1 and VB2 with energy difference of 283 meV) at K point mainly consist of $Mo d$ states. [(b) and (c)] Spin-orbital-projected band structure near K point for the α and β sectors in MoTe_2 , respectively. The dotted lines with different colors denote the band projection onto different spin and orbit states, with $\uparrow(\downarrow)$ indicating the spin projection with the spin polarization axis along the z direction and $d_{x^2-y^2}$ being the majority $Mo d$ state for the plotted bands, illustrating that the inversion partners (α and β sectors) possess opposite local spin polarizations.

Se has smaller SOC than Te). We further project the spin and orbital components of VB1 and VB2 at K valley to illustrate the segregation of spin states. As shown in Figs. 3(b) and 3(c) for the majority orbital ($Mo d_{x^2-y^2}$ state), the spin up (down) states are segregated in the β (α) sector for VB1 at K point, whereas for VB2, the spin up (down) states are in α (β) sector, demonstrating a case of spin-layer locking. Figure S4 [41] shows that the states at K' point have the opposite spin-polarization directions as the corresponding states at K point, which could be related to the experimentally observed opposite spin polarizations at K and K' .

To clearly demonstrate the relationship between the experimentally measured net spin polarization and the potentially hidden spin polarization in MoTe_2 as anticipated from its crystalline symmetry [5], we evaluate the local spin polarizations of the inversion-symmetric α and β sectors in bulk $2H\text{-MoTe}_2$, as shown in Figs. 4(a) and 4(b). The local spin polarizations of each sector is calculated by summing the expectation values of spin operator over the subspace of degenerated states, as the energy bands in $2H\text{-MoTe}_2$ are doubly degenerated per time reversal symmetry and inversion symmetry, thus the evaluated local spin polarization [5] is gauge invariant. As the VB1 and VB2 states measured in experiments are mainly from Mo atoms, we will focus on the symmetry of Mo sites and its related spin polarization. In each $2H\text{-MoTe}_2$ layer (α or β sector), the inversion-asymmetric point group D_{3h} of Mo sites leads to local Dresselhaus spin polarization, as shown by red (blue) arrows for α (β) sector in

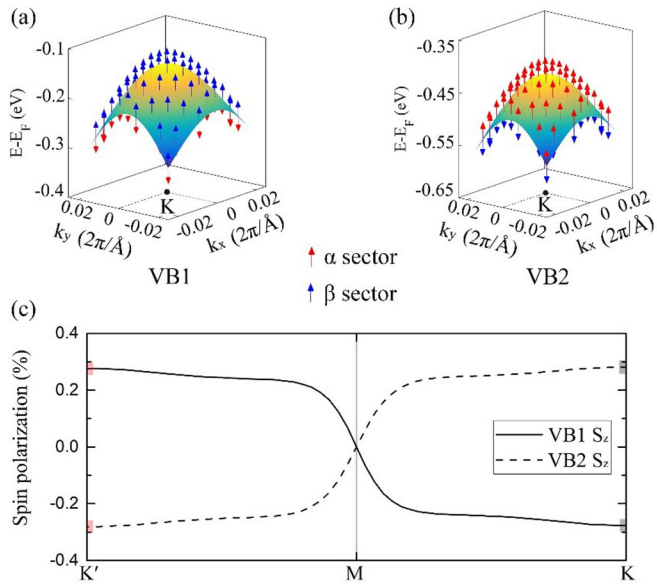


FIG. 4. (a) Projected local spin polarization for VB1 in the K valley of centrosymmetric $2H$ -MoTe₂. Red (blue) arrows denote the spin polarizations on α (β) sector. (b) Projected local spin polarization of VB2. (c) Spin projection with the spin polarization axis along the z direction (S_z) for VB1 and VB2, evaluated from the local spin polarization in bulk $2H$ -MoTe₂ considering the escape depth of photoelectrons. The escape probability of photoelectrons is represented by an exponential function $e^{-\frac{z}{\Delta}}$ with $\Delta = 6 \text{ \AA}$ and z being the distance from the sample surface. The black and red squares indicate the spin polarizations (S_z) at K and K' , respectively.

Figs. 4(a) and 4(b). All the spin polarizations are along out-of-plane directions without helical spin texture, confirming that the spin effects are dominantly related to the Mo sites. The two layers (α and β sectors) in the primitive cell [Fig. 1(b)] possess opposite local spin polarizations, leading to compensated Dresselhaus spin polarization. Although the Te sites in $2H$ -MoTe₂ with C_{3v} point group symmetry could introduce Rashba spin polarization [5], their effect is negligible for VB1 and VB2 at $K(K')$ valley.

The net spin polarization observed in our experiment is the summation of the local spin polarization of the $2H$ -MoTe₂ layers with a set of weights that break the full compensation of local Dresselhaus effects, where the weights are related to the escape depth of photoelectrons. Figure 4(c) shows the spin polarizations (S_z) evaluated from the spin polarization data of α and β sectors shown in Figs. 4(a) and 4(b) for VB1 and VB2, considering the escape depth of photoelectrons [49]. We find that the spin polarizations of VB1 at $K(K')$ are along $-z(z)$ direction, whereas those for VB2 are along $z(-z)$ direction, in agreement with experimental results [Fig. 2(d)]. Both experiment and theory find vanished spin polarization at M point.

To test the effect of surface symmetry breaking in experiments, we have applied a medium dipole field of 50 kV/cm (considering the medium breakdown field of MoTe₂) along z direction in the $2H$ -MoTe₂ structure and calculated the spin polarization of the inversion asymmetric case, as shown in 5(a)–5(d). In the presence of dipole field, the doubly degenerate VB1 (VB2) band splits into singly degenerate VB1_a and

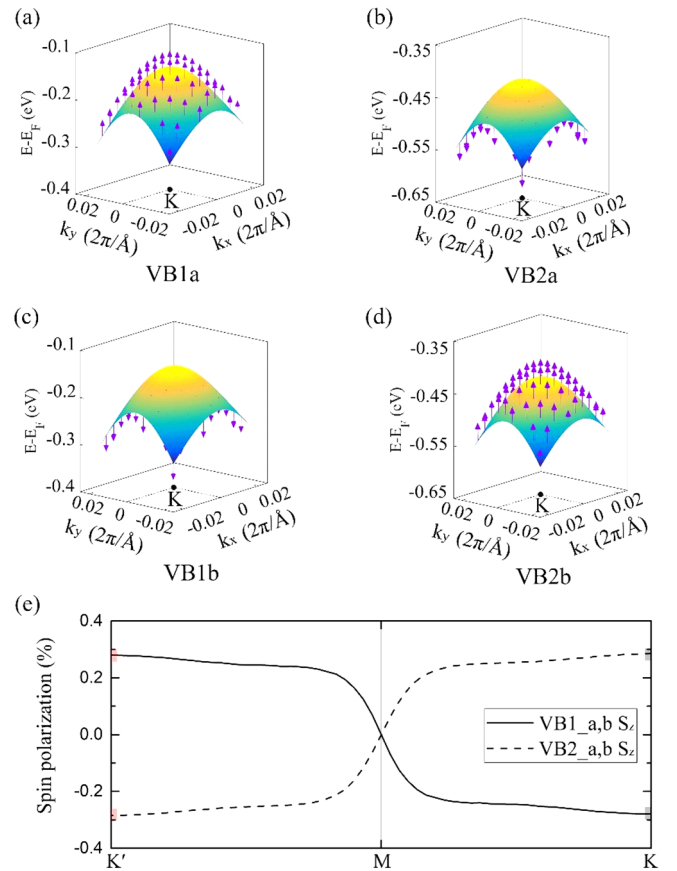


FIG. 5. (a) Spin polarization for the first valence band (VB1_a) in the K valley of $2H$ -MoTe₂ with a medium dipole field (50 kV/cm) applied along z direction to break the inversion symmetry and to split the VB1 (VB2) state in pristine MoTe₂ into nearly degenerate VB1_a and VB1_b (VB2_a and VB2_b) states for considering broken inversion symmetry at the surface in experiments. (b) Spin polarization for VB2_a. [(c) and (d)] Spin polarizations for VB1_b and VB2_b, respectively. (e) Spin projection with the spin polarization axis along the z direction (S_z) for VB1_{a,b} (sum of S_z for VB1_a and VB1_b) and VB2_{a,b} (sum of S_z for VB2_a and VB2_b), evaluated using the same method as in Fig. 4(c) for comparison. The black and red squares indicate the spin polarizations (S_z) at K and K' , respectively.

VB1_b (VB2_a and VB2_b) bands, and each possesses a net spin polarization as demonstrated by the violet arrows. The band structure of $2H$ -MoTe₂ under dipole field is shown in Fig. S5 [41], demonstrating negligible band splitting induced by the dipole field. There is also no visible surface-symmetry-breaking induced band splitting in the experimentally measured band structure [Fig. 2(a)]. After consideration of the escape depth of photoelectrons, we obtained the spin polarization (S_z) data in bulk $2H$ -MoTe₂ under dipole field [Fig. 5(e)], using the same method as for Fig. 4(c) by decomposing the spin polarization onto the two MoTe₂ monolayers in the unit cell. We find that the results in Fig. 5(e) are almost identical with those in Fig. 4(c), confirming that the effect of dipole field mimicked surface symmetry breaking is negligible. We would like to note that, for other material systems with strong surface symmetry breaking effect or large surface dipole field, one can determine the contributions from bulk hidden spin

polarization versus surface symmetry breaking by comparing the calculations with (e.g., Fig. 5) or without (e.g., Fig. 4) dipole field. The surface dipole field and the bulk hidden spin polarization can also induce different fingerprints in spin texture, e.g., helical versus nonhelical spin texture.

V. CONCLUSION

In summary, we have performed spin-ARPES measurements and first-principles evaluations of the spin polarization in $2H$ - MoTe_2 and revealed a hidden Dresselhaus spin polarization in the K and K' valleys with opposite spin textures. Our detailed calculations demonstrate that the effect of symmetry-breaking surface dipole field on spin polarization in the surface sensitive measurements is rather weak as indicated by its negligible contribution to the measured spin polarization and the invisible splitting of energy bands. This shows that the measured spin effects originate from the intrinsic hidden spin polarization in the bulk phase. The large spin splitting and net spin polarization found in spin-ARPES experiments also suggest that the hidden spin effects in inversion symmetric layered compounds can be used to generate large spin splitting on the surfaces in the absence of strong dipole field. Our combinatorial experimental and theoretical studies clarify the existence of hidden spin polarization in the centrosymmetric

materials and opens the way of designing novel functional materials with coexisting hidden spin polarization and other hidden effects, such as hidden orbital polarization [52] and hidden Berry curvature [53], for the energy efficient spintronics applications.

ACKNOWLEDGMENTS

The authors thank Y. Bian for assistance with the XRD measurements. This work is supported by National Key Research and Development Program of China (Grant No. 2016YFA0300803), the National Natural Science Foundation of China (Grants No. 61427812 and No. 11774160), the Natural Science Foundation of Jiangsu Province of China (Grant No. BK20192006), the Fundamental Research Funds for the Central Universities (Grant No. 021014380113), and Shenzhen Science and Technology Innovation Commission (JCYJ20170818093035338, KQTD20170810105439418, JCYJ20170412110137562, and ZDSYS201707271554071). The authors also would like to thank the supports from the Collaborative Innovation Center of Solid State Lighting and Energy-saving Electronics and the Program for high-level Entrepreneurial and Innovative Talent Introduction, Jiangsu Province.

-
- [1] G. Dresselhaus, *Phys. Rev.* **100**, 580 (1955).
 [2] E. I. Rashba, *Sov. Phys. Solid State* **2**, 1109 (1960).
 [3] J. Schaibley and X. Xu, *Nat. Phys.* **10**, 798 (2014).
 [4] J. M. Riley, F. Mazzola, M. Dendzik, M. Michiardi, T. Takayama, L. Bawden, C. Granerød, M. Leandersson, T. Balasubramanian, and M. Hoesch, *Nat. Phys.* **10**, 835 (2014).
 [5] X. Zhang, Q. Liu, J.-W. Luo, A. J. Freeman, and A. Zunger, *Nat. Phys.* **10**, 387 (2014).
 [6] L. Yuan, Q. Liu, X. Zhang, J. W. Luo, and A. Zunger, *Nat. Commun.* **10**, 906 (2019).
 [7] R. Winkler, *Spin-Orbit Coupling Effects in Two-Dimensional Electron and Hole Systems* (Springer-Verlag, Berlin, Heidelberg, 2003).
 [8] H. Yuan, Z. Liu, G. Xu, B. Zhou, S. Wu, D. Dumcenco, K. Yan, Y. Zhang, S.-K. Mo, and P. Dudin, *Nano Lett.* **16**, 4738 (2016).
 [9] W. Jin, P.-C. Yeh, N. Zaki, D. Zhang, J. T. Sadowski, A. Al-Mahboob, A. M. van Der Zande, D. A. Chenet, J. I. Dadap, I. P. Herman *et al.*, *Phys. Rev. Lett.* **111**, 106801 (2013).
 [10] J. A. Miwa, M. Dendzik, S. S. Grønberg, M. Bianchi, J. V. Lauritsen, P. Hofmann, and S. Ulstrup, *ACS Nano* **9**, 6502 (2015).
 [11] J. A. Miwa, S. Ulstrup, S. G. Sørensen, M. Dendzik, A. G. Čabo, M. Bianchi, J. V. Lauritsen, and P. Hofmann, *Phys. Rev. Lett.* **114**, 046802 (2015).
 [12] W. Zhao, R. M. Ribeiro, M. Toh, A. Carvalho, C. Kloc, A. Castro Neto, and G. Eda, *Nano Lett.* **13**, 5627 (2013).
 [13] M. M. Ugeda, A. J. Bradley, Y. Zhang, S. Onishi, Y. Chen, W. Ruan, C. Ojeda-Aristizabal, H. Ryu, M. T. Edmonds, and H.-Z. Tsai, *Nat. Phys.* **12**, 92 (2016).
 [14] L. Bawden, S. Cooil, F. Mazzola, J. Riley, L. Collins-McIntyre, V. Sunko, K. Hunvik, M. Leandersson, C. Polley, and T. Balasubramanian, *Nat. Commun.* **7**, 11711 (2016).
 [15] Y. Liu, N. O. Weiss, X. Duan, H.-C. Cheng, Y. Huang, and X. Duan, *Nat. Rev. Mater.* **1**, 16042 (2016).
 [16] H. Zeng, J. Dai, W. Yao, D. Xiao, and X. Cui, *Nat. Nano* **7**, 490 (2012).
 [17] K. F. Mak, K. He, J. Shan, and T. F. Heinz, *Nat. Nano* **7**, 494 (2012).
 [18] F. Bussolotti, H. Kawai, Z. E. Ooi, V. Chellappan, D. Thian, A. L. C. Pang, and K. E. J. Goh, *Nano Futures* **2**, 032001 (2018).
 [19] Y. Zhang, M. M. Ugeda, C. Jin, S.-F. Shi, A. J. Bradley, A. Martín-Recio, H. Ryu, J. Kim, S. Tang, and Y. Kim, *Nano Lett.* **16**, 2485 (2016).
 [20] J. M. Riley, W. Meevasana, L. Bawden, M. Asakawa, T. Takayama, T. Eknapakul, T. Kim, M. Hoesch, S.-K. Mo, and H. Takagi, *Nat. Nano* **10**, 1043 (2015).
 [21] G. Wang, C. Robert, A. Suslu, B. Chen, S. Yang, S. Alamdari, I. C. Gerber, T. Amand, X. Marie, and S. Tongay, *Nat. Commun.* **6**, 10110 (2015).
 [22] R. Suzuki, M. Sakano, Y. Zhang, R. Akashi, D. Morikawa, A. Harasawa, K. Yaji, K. Kuroda, K. Miyamoto, and T. Okuda, *Nat. Nano* **9**, 611 (2014).
 [23] D. Xiao, G.-B. Liu, W. Feng, X. Xu, and W. Yao, *Phys. Rev. Lett.* **108**, 196802 (2012).
 [24] Y. Ye, J. Xiao, H. Wang, Z. Ye, H. Zhu, M. Zhao, Y. Wang, J. Zhao, X. Yin, and X. Zhang, *Nat. Nano* **11**, 598 (2016).
 [25] M. Gehlmann, I. Aguilera, G. Bihlmayer, E. Młyńczak, M. Eschbach, S. Döring, P. Gospodarič, S. Cramm, B. Kardynał, and L. Plucinski, *Sci. Rep.* **6**, 26197 (2016).
 [26] W. Yao, E. Wang, H. Huang, K. Deng, M. Yan, K. Zhang, K. Miyamoto, T. Okuda, L. Li, and Y. Wang, *Nat. Commun.* **8**, 14216 (2017).
 [27] E. Razzoli, T. Jaouen, M.-L. Mottas, B. Hildebrand, G. Monney, A. Pisoni, S. Muff, M. Fanciulli, N. C. Plumb, V. A. Rogalev *et al.*, *Phys. Rev. Lett.* **118**, 086402 (2017).

- [28] A. P. Weber, P. Rübmann, N. Xu, S. Muff, M. Fanciulli, A. Magrez, P. Bugnon, H. Berger, N. C. Plumb, M. Shi *et al.*, *Phys. Rev. Lett.* **121**, 156401 (2018).
- [29] A. M. Jones, H. Yu, J. S. Ross, P. Klement, N. J. Ghimire, J. Yan, D. G. Mandrus, Y. Wang, and X. Xu, *Nat. Phys.* **10**, 130 (2014).
- [30] Q. Liu, X. Zhang, and A. Zunger, *Phys. Rev. Lett.* **114**, 087402 (2015).
- [31] M. Brotons-Gisbert, A. Segura, R. Robles, E. Canadell, P. Ordejón, and J. F. Sánchez-Royo, *Phys. Rev. Mater.* **2**, 054602 (2018).
- [32] P. Li and I. Appelbaum, *Phys. Rev. B* **97**, 125434 (2018).
- [33] J. Jiang, Z. K. Liu, Y. Sun, H. F. Yang, C. R. Rajamathi, Y. P. Qi, L. X. Yang, C. Chen, H. Peng, and C. C. Hwang *et al.*, *Nat. Commun.* **8**, 13973 (2017).
- [34] J. R. Schaibley, H. Yu, G. Clark, P. Rivera, J. S. Ross, K. L. Seyler, W. Yao, and X. Xu, *Nat. Rev. Mater.* **1**, 16055 (2016).
- [35] Y. Wang, J. Xiao, H. Zhu, Y. Li, Y. Alsaïd, K. Y. Fong, Y. Zhou, S. Wang, W. Shi, Y. Wang *et al.*, *Nature* **550**, 487 (2017).
- [36] D. H. Keum, S. Cho, J. H. Kim, D.-H. Choe, H.-J. Sung, M. Kan, H. Kang, J.-Y. Hwang, S. W. Kim, H. Yang *et al.*, *Nat. Phys.* **11**, 482 (2015).
- [37] S. Cho, S. Kim, J. H. Kim, J. Zhao, J. Seok, D. H. Keum, J. Baik, D.-H. Choe, K. Chang, and K. Suenaga, *Science* **349**, 625 (2015).
- [38] J. A. Wilson and A. D. Yoffe, *Adv. Phys.* **18**, 193 (1969).
- [39] Y. Zhang, T.-R. Chang, B. Zhou, Y.-T. Cui, H. Yan, Z. Liu, F. Schmitt, J. Lee, R. Moore, Y. Chen *et al.*, *Nat. Nano* **9**, 111 (2013).
- [40] Z. Gong, G.-B. Liu, H. Yu, D. Xiao, X. Cui, X. Xu, and W. Yao, *Nat. Commun.* **4**, 2053 (2013).
- [41] See Supplemental Material at <http://link.aps.org/supplemental/10.1103/PhysRevB.101.035102> for detailed information about experimental geometry, theoretical methods and additional figures. References [42–48] are also included.
- [42] W. Kohn and L. J. Sham, *Phys. Rev.* **140**, A1133 (1965).
- [43] G. Kresse and J. Furthmüller, *Comput. Mater. Sci.* **6**, 15 (1996).
- [44] G. Kresse and D. Joubert, *Phys. Rev. B* **59**, 1758 (1999).
- [45] J. P. Perdew, K. Burke, and M. Ernzerhof, *Phys. Rev. Lett.* **77**, 3865 (1996).
- [46] M. Dion, H. Rydberg, E. Schröder, D. C. Langreth, and B. I. Lundqvist, *Phys. Rev. Lett.* **92**, 246401 (2004).
- [47] J. Klimeš, D. R. Bowler, and A. Michaelides, *Phys. Rev. B* **83**, 195131 (2011).
- [48] P. Błoński and J. Hafner, *Phys. Rev. B* **79**, 224418 (2009).
- [49] M. P. Seah and W. Dench, *Surf. Interface Anal.* **1**, 2 (1979).
- [50] U. Heinzmann and J. H. Dil, *J. Phys.: Condens. Matter* **24**, 173001 (2012).
- [51] J. Osterwalder, *J. Phys.: Condens. Matter* **24**, 171001 (2012).
- [52] J. H. Ryoo and C.-H. Park, *Npg Asia Materials* **9**, e382 (2017).
- [53] S. Cho, J.-H. Park, J. Hong, J. Jung, B. S. Kim, G. Han, W. Kyung, Y. Kim, S. K. Mo, J. D. Denlinger *et al.*, *Phys. Rev. Lett.* **121**, 186401 (2018).